Supplementary Information (SI) for Journal of Materials Chemistry C.

Supplementary Information

For

Intermolecular Charge-Transfer Phosphorescence in Organometallic-Organic Doped Crystals Dominated by Iridium Complex Lattice

Jiaxuan Wang,[a#] Heming Zhang,[a#] Lianbao Ke,[a] Baoyan Liang,[a] Zhiqiang Li,[a] Semion K. Saikin,[b*] Yue Wang,[a,c] Hai Bi[a*]

a. Jihua Laboratory, 28 Huandaonan road, Nanhai district, Foshan, Guangdong Province, China.
b. Kebotix, Inc., 501 Massachusetts Avenue, Cambridge, MA 02139, USA
c. State Key Laboratory of Supramolecular Structure and Materials, College of Chemistry, Jilin University, Changchun 130012, P. R. China.

[#] These authors contributed equally.

Contents

S1. General information.

All the reagents and solvents were obtained from commercial sources and directly used without any further purification. Morphology of materials was observed using an Olympus fluorescence microscope with UV light source and a Thermo Scientific Prisma E SEM. XRD diffraction spectra were measured by a Bruker D8 Advance instrument. Ultraviolet-visible absorption spectra were measured by a Hitachi UV-vis spectrophotometer using an integrating sphere. Cryogenic measurements (e.g., temperature-dependent photoluminescence spectra and time-resolved emission decay) were performed using a liquid cryogen optical cryostat for spectroscopy (OXFORD INSTRUMENTS: OptistatDN). The samples were mounted in a sample holder, and liquid nitrogen was used as a liquid cryogen to maintain a constant temperature of 77 K. The PL spectra were measured by Edinburgh fluorescence spectrometer (FLS1000) equipped with a xenon arc lamp. The time-resolved emission decay were measured using FLS1000 fluorescence lifetime measurement system with LED excitation sources and a microsecond flash-lamp. Temperature-dependent time-resolved emission decay were investigated under vacuum using FLS1000 fluorescence lifetime measurement system with a microsecond flash-lamp. The transient absorption spectra were carried out on Femtosecond transient absorption spectrometer (Helios Fire).

High-performance liquid chromatography (HPLC) analysis was conducted using a COSMOSIL Cholester column with a 4.6 mm inner diameter, 250 mm length, and 5 μm packing material. The column temperature was maintained at 40 °C, and the mobile phase consisted of tetrahydrofuran and water in a 6:4 (v/v) ratio. An injection volume of 10 μL was used, and detection was performed at a wavelength of 254 nm. We prepared a series of pure QPO and pure $Ir(ppy)_2(acac)$ solutions with known concentrations (ranging from 0.1 to 1.0 mg/mL for $Ir(ppy)_2(acac)$; 0.005 to 0.01 mg/mL for QPO) in HPLC-grade tetrahydrofuran. Each solution was measured in triplicate to ensure reproducibility. For each compound, we plotted the integrated HPLC peak area (at 254 nm) against its known concentration, yielding two separate linear calibration curves:

$$\text{QPO: } y = 5.768972\times10^{7}x-2.787670\times10^{4}\ (R^2 = 0.999);$$

$$Ir(ppy)_2(acac)\text{: } y = 3.530333\times10^{7}x-3.421406\times10^{5}\ (R^2 = 0.999),$$

where y = peak area and x = concentration (mg/mL).For each Q-Ir crystal sample, we now calculate QPO and $Ir(ppy)_2(acac)$ concentrations individually using their respective calibration curves and then determine the molar ratio.

Powder X-ray diffraction (PXRD) measurements were performed using a diffractometer equipped with a theta/theta vertical goniometer. The X-ray source was a Cu target with a standard-size optical tube. A Lynxeye XE-T energy-dispersive array detector was used for data collection. The 2Theta angle range covered was 5° to 60°, with an angular accuracy of 0.0001 degrees. Samples were mounted on a quartz sample holder.

S2. Sample fabrication.

QPO was synthesized following the standard reaction route from literature (Scheme S1). Ir(ppy)$_2$(acac) was purchased from Bidepharm.

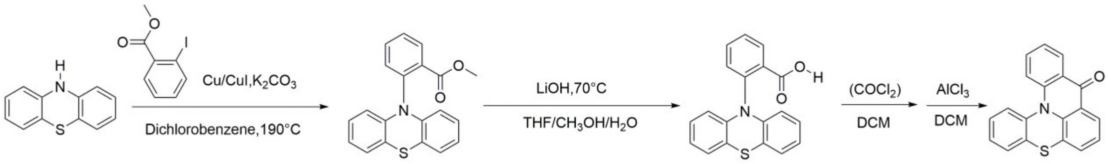

Scheme S1. Synthesis of QPO.[1]

Engineered crystals composed of Ir(ppy)$_2$(acac) host and QPO guest molecules were fabricated using a modified bilayer-film annealing method.[2] Initially, QPO was deposited onto a piece of clear quartz. The amorphous QPO film gradually transformed into a crystalline film at a low temperature of 333 K. Subsequently, Ir(ppy)$_2$(acac) was sequentially deposited onto the crystallized QPO layer. The problem of the large difference in sublimation temperatures of the two components is solved via the crystallization of QPO layer. Both the QPO and Ir(ppy)$_2$(acac) layers had a thickness of 100 nm. A piece of clear quartz was then placed over the QPO: Ir(ppy)$_2$(acac) bilayer film. The Q-Ir crystals were formed at an annealing temperature of 493 K for ten minutes. Due to the temperature difference between the upper and lower quartz plates during bilayer-film annealing process, the QPO crystallized on the upper quartz plate after underwent sublimation (Figure S4). The Q-Ir doped crystals on the quartz sheet below exhibit a final doping yield of 1–6%, which reflects the fraction of QPO successfully incorporated into the host lattice. The samples of individual QPO and Ir(ppy)$_2$(acac) were prepared in the same method. Both the thickness of QPO film and Ir(ppy)$_2$(acac) film is 100 nm. For the growth of pure

$Ir(ppy)_2(acac)$ single crystals, the traditional sublimation crystallization method was employed.

By adjusting the thickness of the organic layer, the concentration of QPO in the crystal can be effectively adjusted from 0.7% to 4.3% while keeping the heating temperature and heating time unchanged.

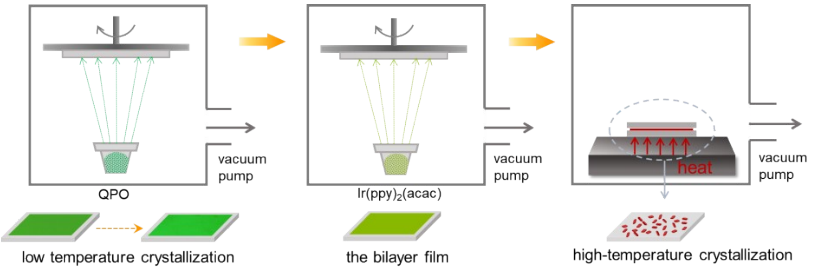

Scheme S2. The preparation process of engineered crystal.

S3. Computational details.

The computational model is a double-level structure with a QPO-Ir dimer in the center as the high-level and $Ir(ppy)_2(acac)$ molecules as the surrounding low-level. The guest QPO molecule was inserted into the crystalline matrix of the $Ir(ppy)_2(acac)$. The coordinates of the molecules in the corner were fixed and other molecules were relaxed. The optimization and frequency computations of the high level were conducted using density functional theory[3] (DFT) with PBE0[4]-D3BJ[5]/def2-SVP[6] supported by Gaussian 16 C.02 version[7]. The convergency of the geometry and energy are at "tight" level (1.5×10^{6} a.u energy for self-consistent field, 1.5×10^{8}a.u. for root-mean-square (RMS) density matrix, 1.5×10^{5} a.u. for maximum Force, 1.0×10^{5} a.u. for RMS Force, 6.0×10^{5} a.u. for maximum displacement, 4.0×10^{5} a.u. for RMS displacement). The excitation energies were computed using time depended density functional theory[8] (TD-DFT) with PBE0-D3BJ/def2-TZVPP[6]. The single point calculations were done using the def2-TZVPP basis set. The optimization of the low-level is carried out by xtb-GFN2[9] as a semiempirical quantum chemistry method.

Seven geometries of conformers were created by replacing one QPO molecule with one $Ir(ppy)_2(acac)$ molecule in the crystal cluster and then adjusting the orientation of the QPO molecule in the principle of forming intermolecular interactions including hydrogen bonding, hydrogen-π interaction, and π-π stacking. These three type of interactions, especially the hydrogen bonding, are the most important intermolecular interactions for charge transfer property and they are preferred. Then the initial geometries were optimized to obtain converged stuctures. According to the symmetric arrangement of the $Ir(ppy)_2(acac)$ molecules in the crystal and the possible number of the hydrogen bonding, hydrogen-π interaction, and π-π stacking, the interaction sites were selected. The conformer with the largest binding energy was selected as the model for the following computations. The spectrum of the phosphorescence was computed using MOMAP program[10].

S4. Supplementary Experimental Figures and Tables

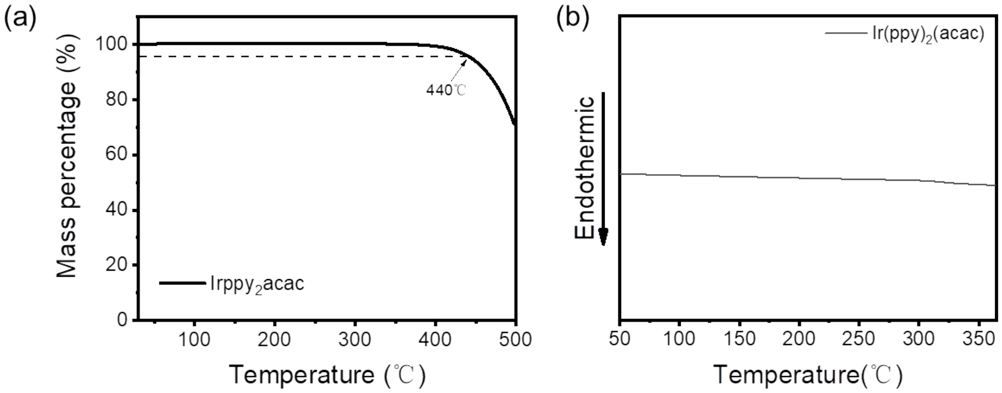

Figure S1. The TGA (**a**) and DSC (**b**) curve analysis of $Ir(ppy)_2(acac)$.

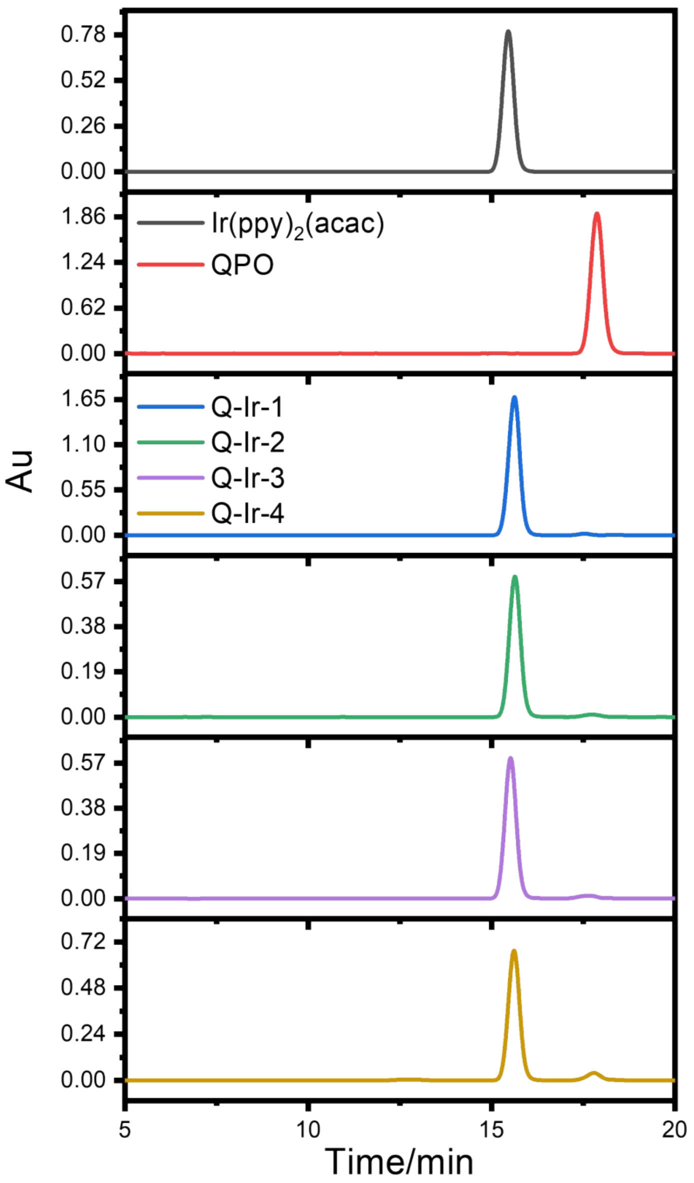

Figure S2. The high-performance liquid chromatography of QPO, Ir(ppy)$_2$(acac), and Q-Ir crystal with different doping concentrations.

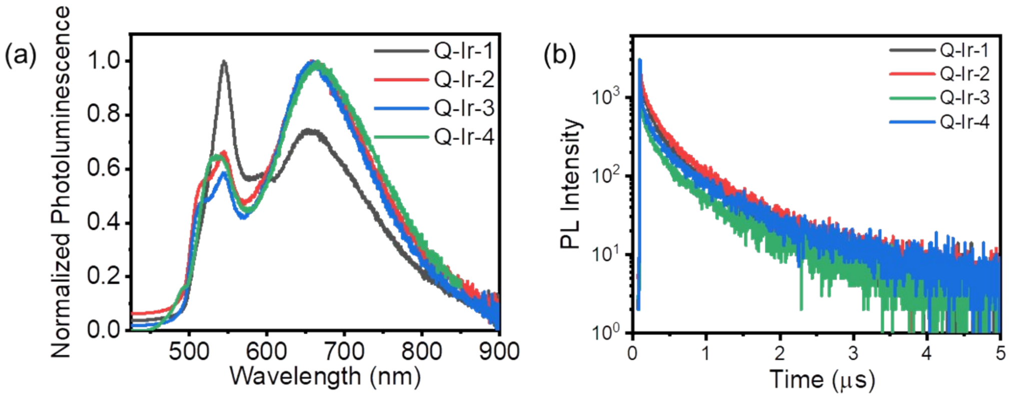

Figure S3. The PL spectra (**a**) and time-resolved emission decay curves (**b**) of crystals with different concentrations.

Table S1. The purity of QPO and Ir(ppy)$_2$(acac).

QPO	99.83%
Ir(ppy)$_2$(acac)	99.78%

Table S2. Sample preparation conditions and corresponding concentrations.

Doped crystal	Q-Ir-1	Q-Ir-2	Q-Ir-3	Q-Ir-4
Thickness of QPO/nm	50	100	150	200
Thickness of Ir(ppy)$_2$(acac)/nm	100	100	100	100
Concentration of QPO	0.73	1.69	2.05	4.27

Table S3. The PLQY of doped crsytal with different doping concentrations.

	PLQY
QPO crystals	19.4
Ir(ppy)$_2$(acac) crystals	0.5
Q-Ir-1	0.6
Q-Ir-2	1.7
Q-Ir-3	0.9
Q-Ir-4	0.7

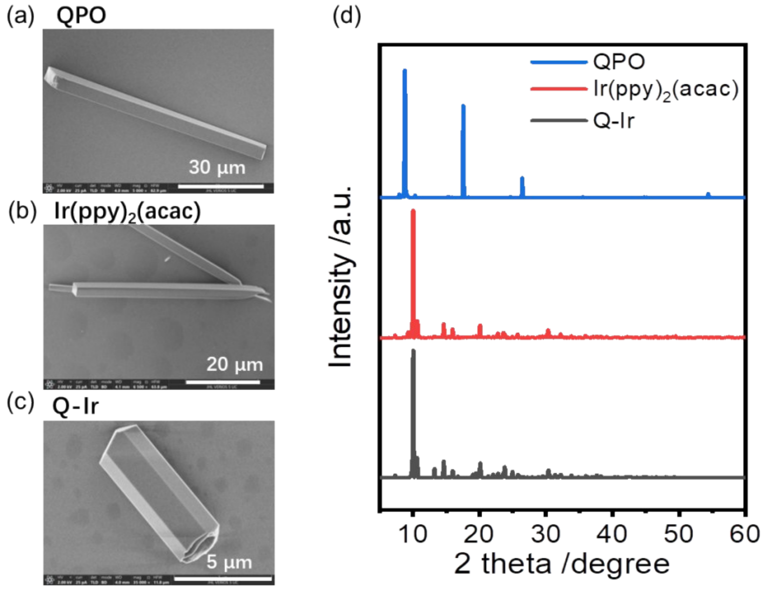

Figure S4. Scanning electron microscope (SEM) images of QPO (**a**), Ir(ppy)$_2$(acac) (**b**), and Q-Ir crystal (**c**). X-ray diffraction patterns of the engineered crystal and single-component QPO and Ir(ppy)$_2$(acac) crystals (**d**).

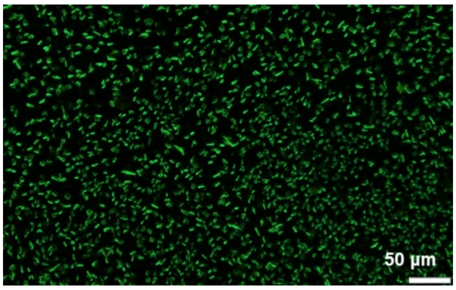

Figure S5. fluorescence microscope image of the QPO crystals in the quartz plate placed above.

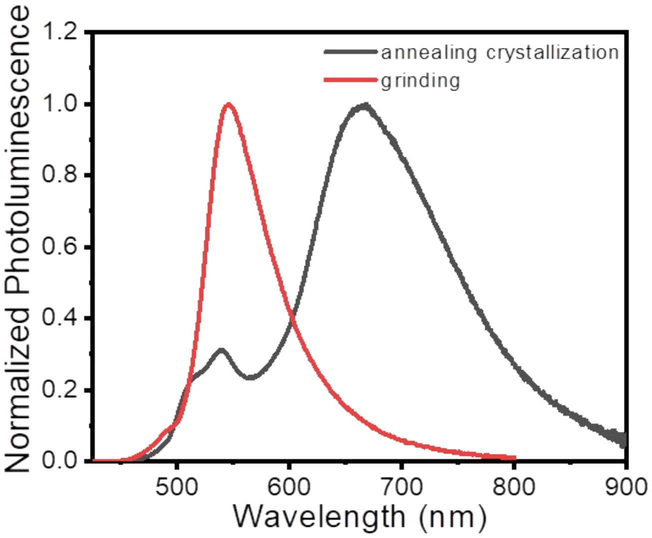

Figure S6. The PL spectra of QPO and Ir(ppy)$_2$(acac) grinding mixtures and doped crystals obtained through annealing crystallization.

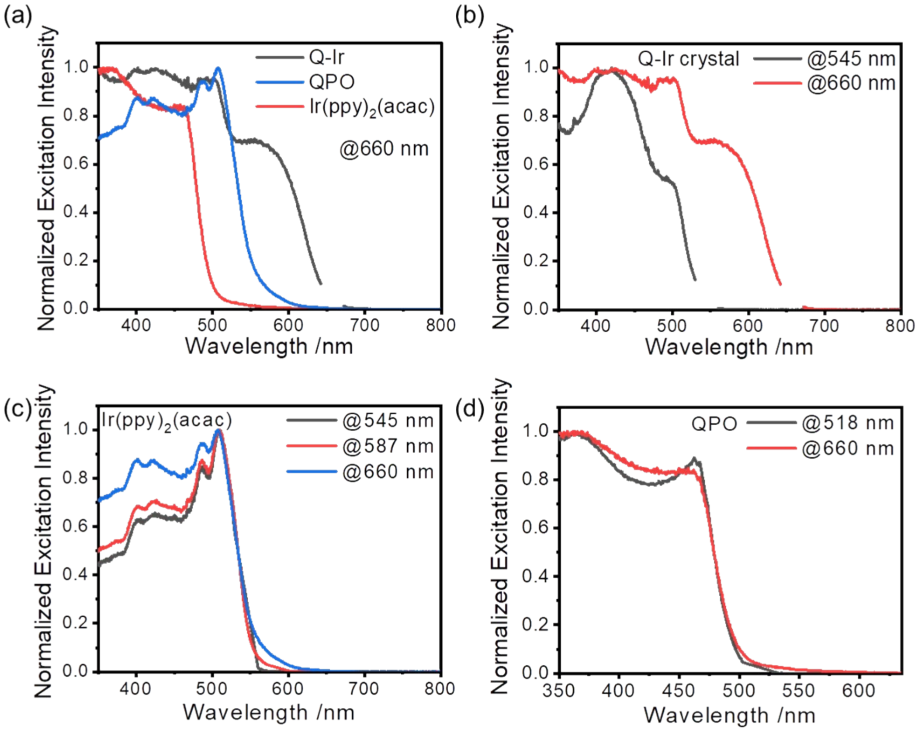

Figure S7. Excitation spectra of QPO, Ir(ppy)$_2$(acac), and Q-Ir crystal detected at 660 nm (**a**). Excitation spectra of Q-Ir crystal detected at 545 and 660 nm (**b**). Excitation spectra of Ir(ppy)$_2$(acac) crystal detected at 545, 587, and 660 nm (**c**). Excitation spectra of QPO crystal detected at 518 and 660 nm (**d**).

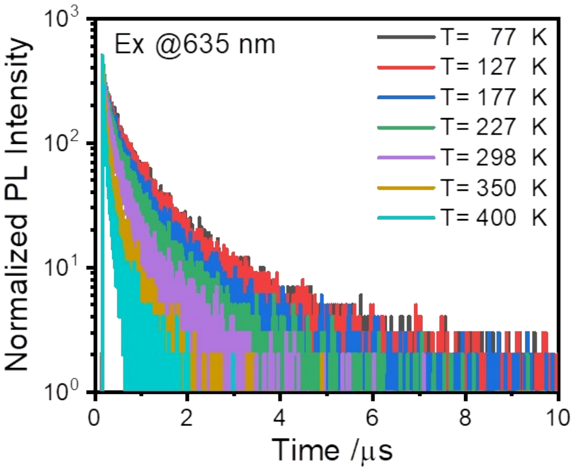

Figure S8. Temperature-dependent time-resolved emission decay curves of Q-Ir crystal under 635 nm excitation, detected at 670 nm.

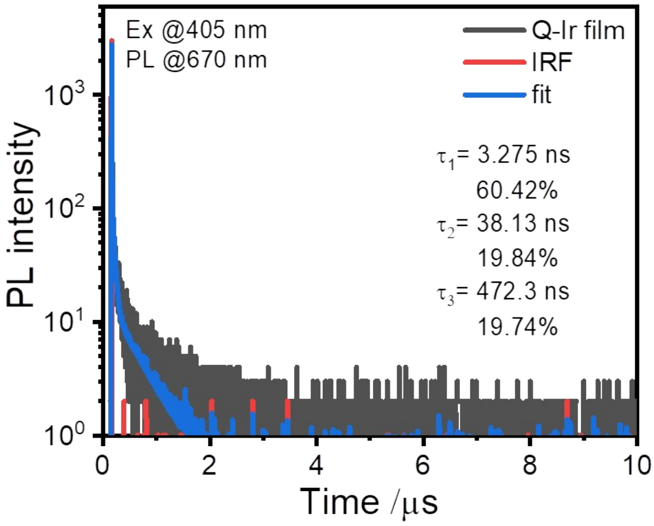

Figure S9. The time-resolved emission decay of the amorphous film composed of Ir(ppy)$_2$(acac) and QPO measured at 670 nm.

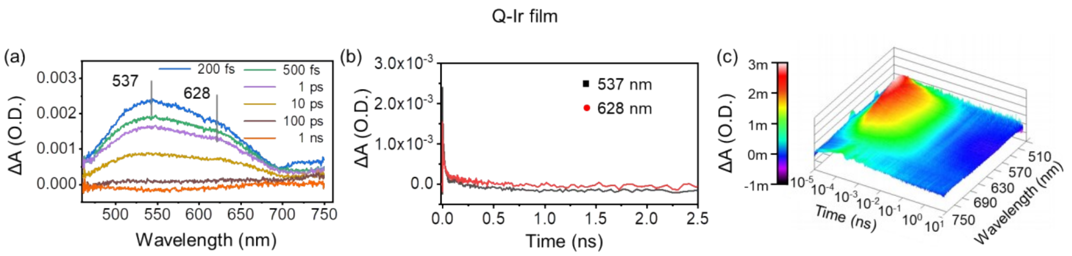

Figure S10. The transient absorption spectra (**a**), the decay profiles (**b**), and the 3D color plots of transient absorption spectra (**c**) of Q-Ir film in the range of 490-750 nm.

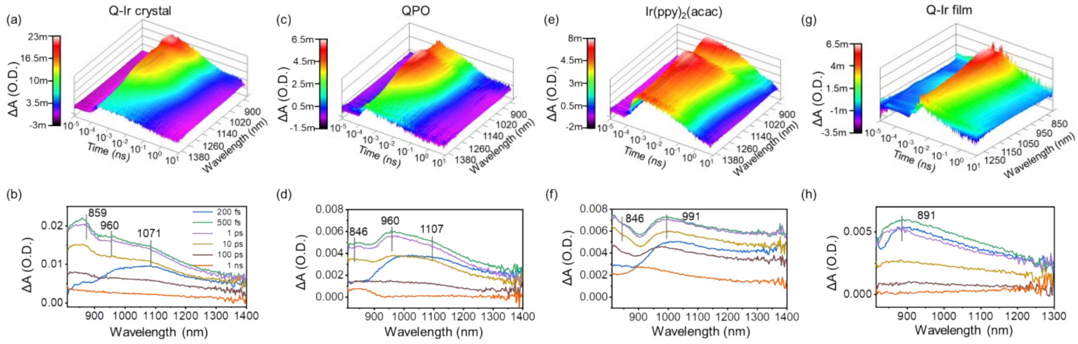

Figure S11. The 3D color plots of transient absorption spectra and transient absorption spectra of Q-Ir crystal (**a**,**b**), QPO (**c**,**d**), Ir(ppy)$_2$(acac) (**e**,**f**), and Q-Ir film (**g**,**h**) in the range of 810-1400 nm.

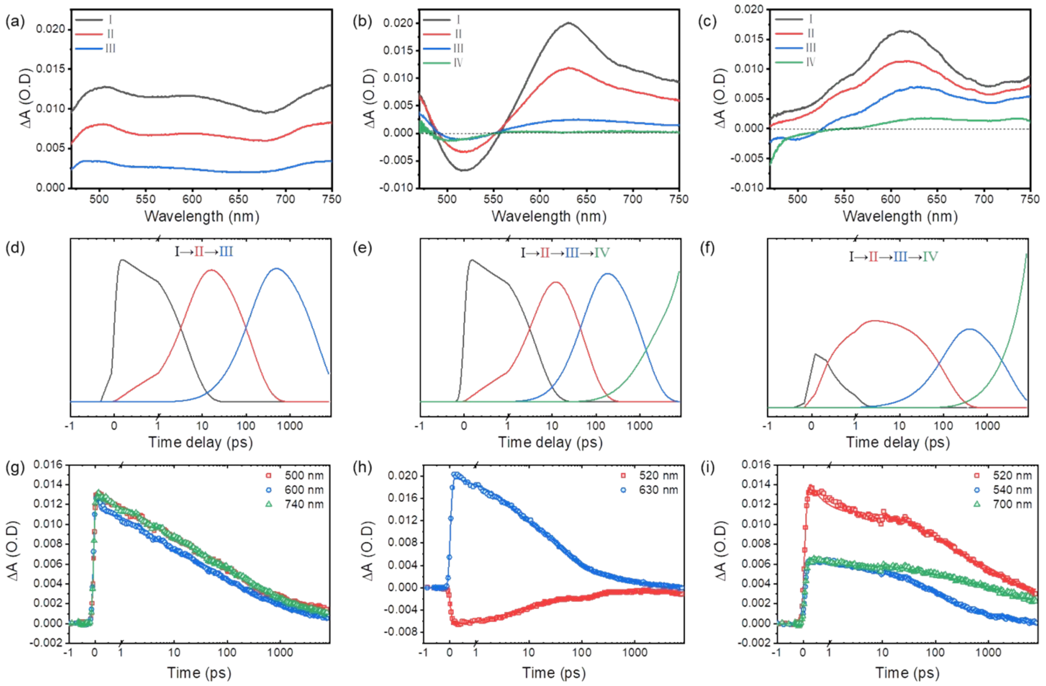

Figure S12. Target-analysis-extracted species associated spectra (SAS) of Ir(ppy)$_2$(acac) (**a**), QPO (**b**), Q-Ir crystal (**c**); Target-analysis-extracted concentration evolution of transient species for Ir(ppy)$_2$(acac) (**d**), QPO (**e**), Q-Ir crystal (**f**); Time traces (open circles) and fitting curves (solid lines) by target analysis of the fs-TA at selected probe wavelengths for Ir(ppy)$_2$(acac) (**g**), QPO (**h**), Q-Ir crystal (**i**).

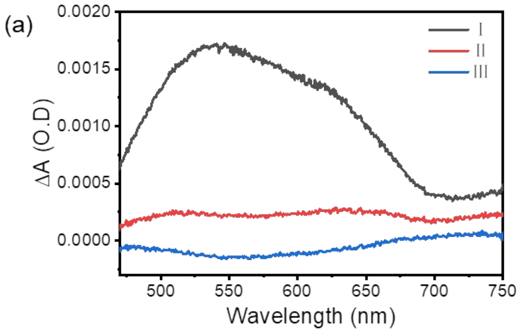

Figure S13. Target-analysis-extracted species associated spectra (SAS) (**a**) and target-analysis-extracted concentration evolution of transient species (**b**) of Q-Ir film.

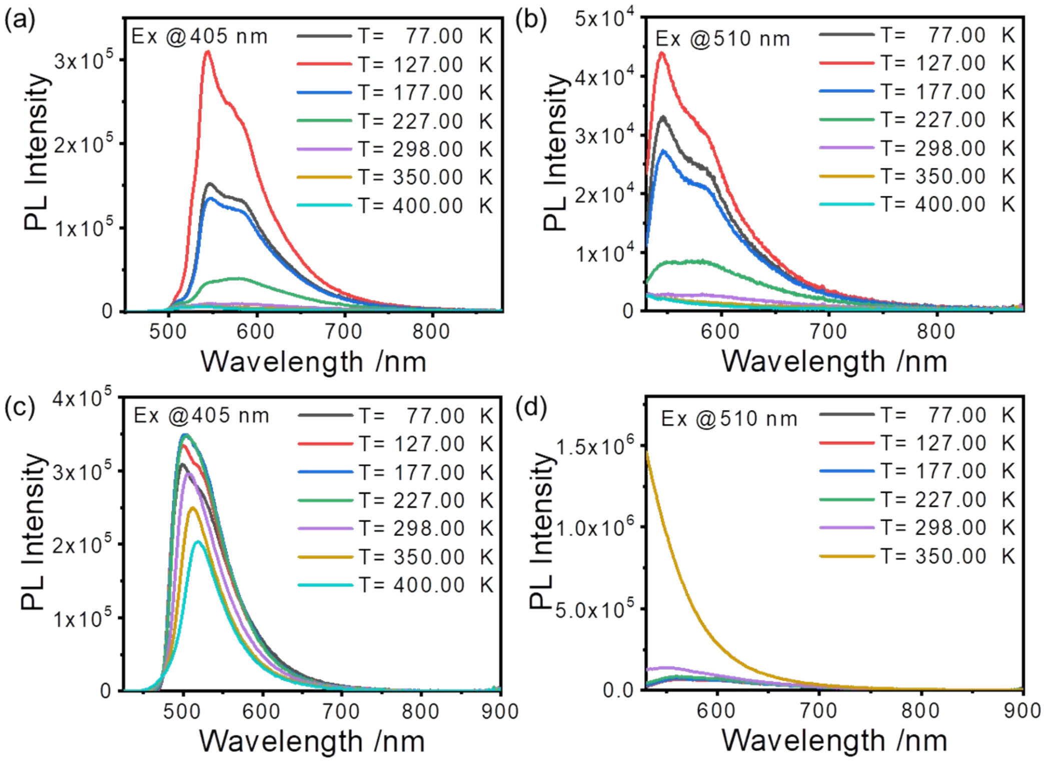

Figure S14. Temperature-dependent PL spectra of Ir(ppy)$_2$(acac) under 405 nm (**a**) and 510 nm (**b**) excitation. Temperature-dependent PL spectra of QPO under 405 nm (**c**) and 510 nm (**d**) excitation.

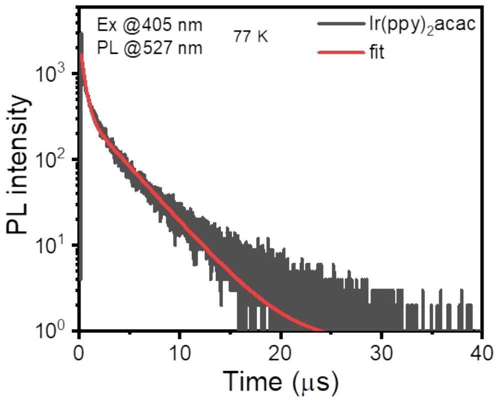

Figure S15. The time-resolved emission decay of Ir(ppy)$_2$(acac) at 77 K.

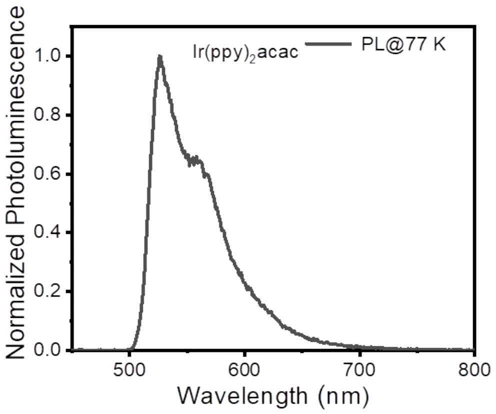

Figure S16. The photoluminescence spectra of Ir(ppy)$_2$(acac) crystal at 77 K.

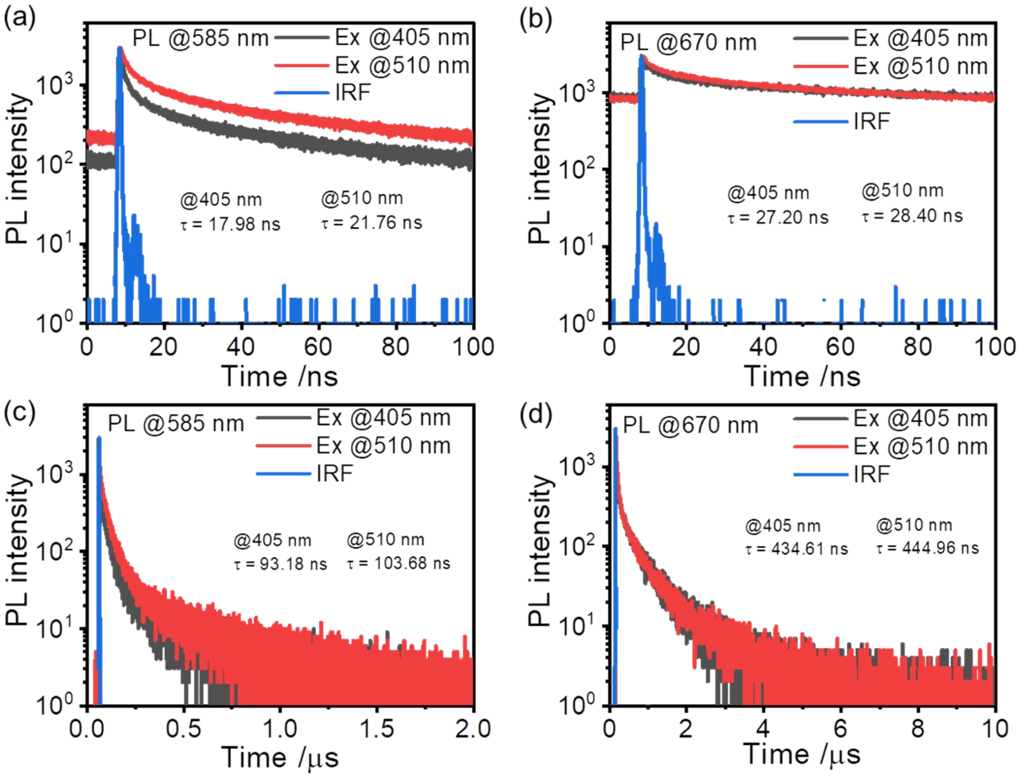

Figure S17. The time-resolved emission decay curves of Ir(ppy)$_2$(acac) under 405 nm and 510 nm excitation. (**a**) emission at 585 nm over a timeframe of 100 ns, (**b**) emission at 670 nm over a timeframe of 100 ns, (**c**) emission at 585 nm over a timeframe of 2 μs, and (**d**) emission at 670 nm over a timeframe of 10μs.

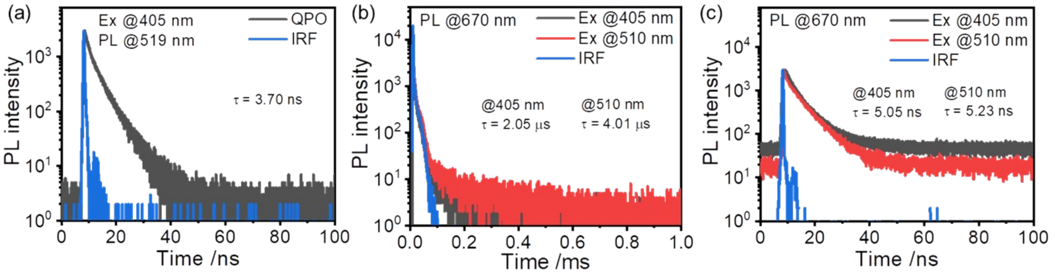

Figure S18. The time-resolved emission decay curves of QPO under 405 nm and 510 nm excitation. (**a**) emission at 519 nm over a timeframe of 100 ns, (**b**) emission at 670 nm over a timeframe of 1 ms, (**c**) emission at 670 nm over a timeframe of 100 ns.

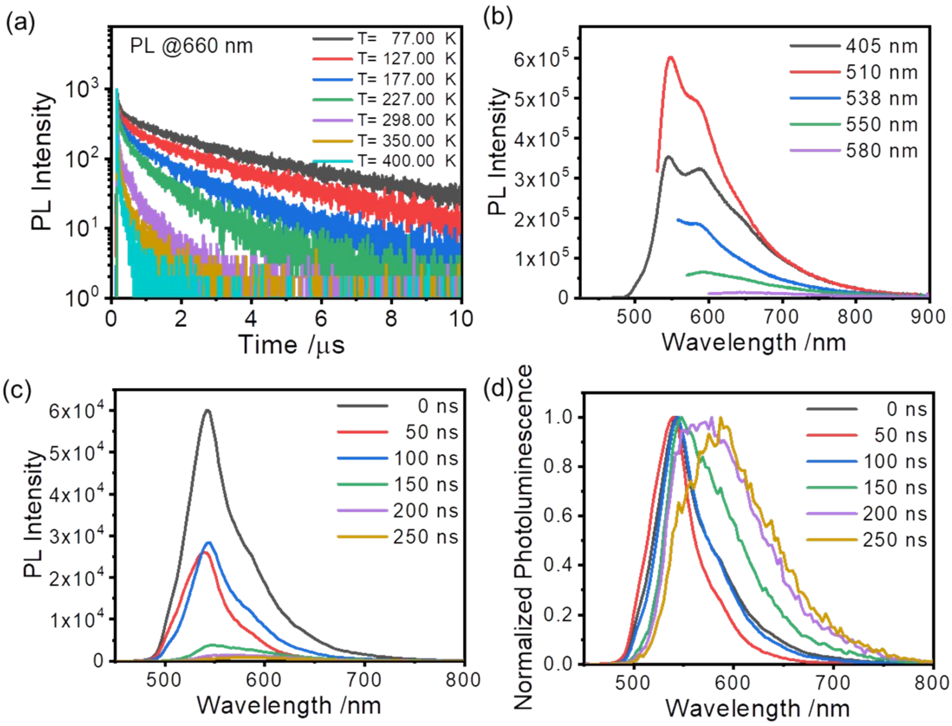

Figure S19. The temperature-dependent time-resolved emission decay curves of Ir(ppy)$_2$(acac) (**a**). The PL spectra of Ir(ppy)$_2$(acac) under 405, 510, 538, 550, and 580 nm excitation (**b**). The time-dependent PL spectra of Ir(ppy)$_2$(acac) (**c,d**).

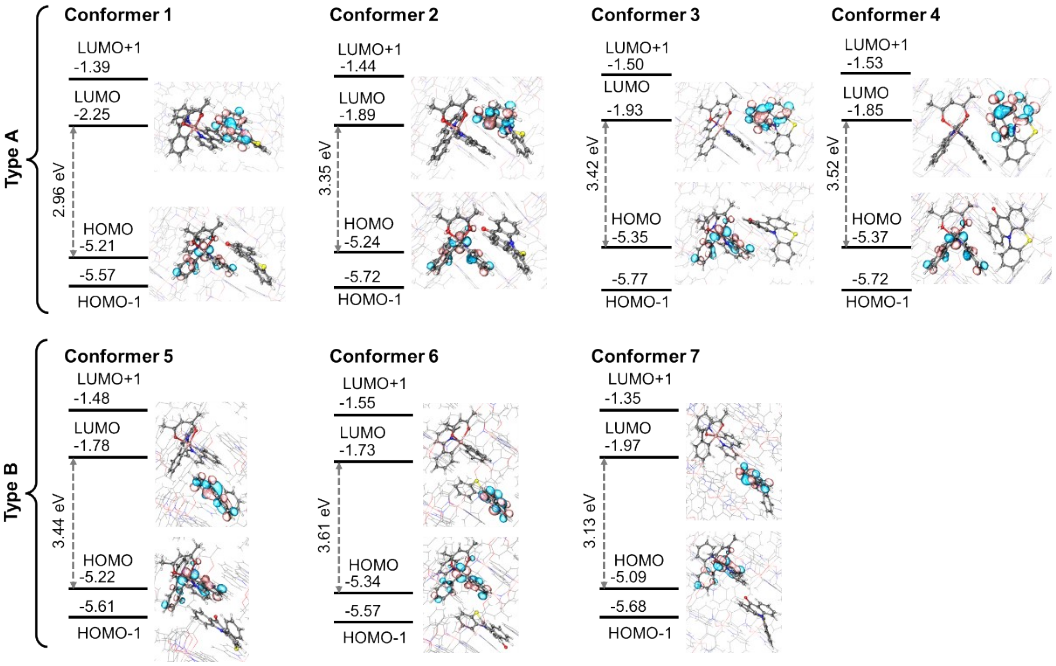

Figure S20. The energy levels and frontier molecular orbitals of the different conformers.

Table S4. Binding energies of each calculated conformer.

	Type A				Type B		
Conformer	1	2	3	4	5	6	7
binding energy / kJ mol^{-1}	-62.9	-56.8	-54.9	-52.6	-66.9	-65.1	-38.8

Seven distinct conformers were studied. Their geometry and energy levels are shown in Figure S22. These conformers are classified into two types according to the different intermolecular interaction sites. Type A is involved with the interaction with the acetylacetonato and a phenyl-pyridinyl groups and Type B is involved with the two phenyl-pyridinyl groups. Generally, for all the conformers show intermolecular charge transfer characteristics between the LUMO and HOMO. The difference is the HOMO-LUMO gap. For Type A, when the binding energy increases (becoming more negative) as listed in Table S1, the gap tends to decrease. Tighter intermolecular interactions can be beneficial for the intermolecular charge transfer transition. While, for Type B, the binding energies of Conformer 5 and 6 is larger than that of Conformer 1, but the gaps are much larger than Conformer 1. Thus, the interaction site is also important for the intermolecular charge transfer transition. Within the scale of our research the interaction with the acetylacetonato group is more effective to lower the gap to realize the red-shifted emission. We have also calculated the phosphorescence spectra of the conformers in Type A as shown in Figure S23. Conformer 1 shows the obvious red-shifted emission which is coherent with the experimental results.

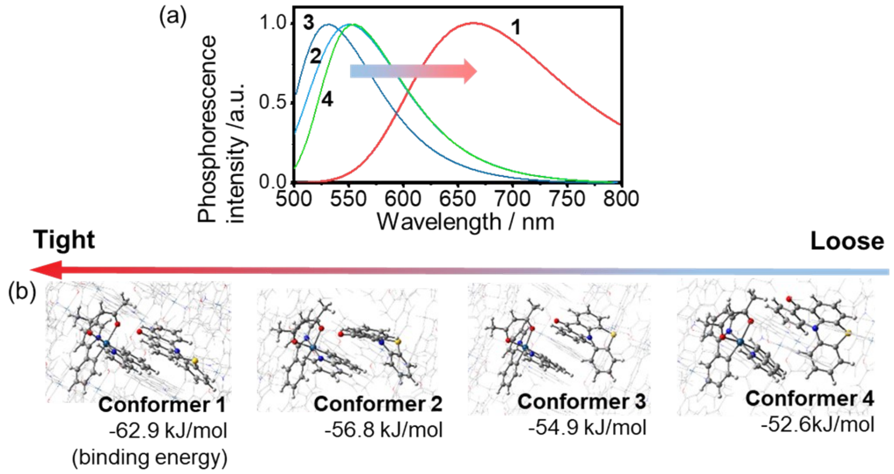

Figure S21. The calculated conformer 1-4, and the calculated binding energies of conformer 1-4.

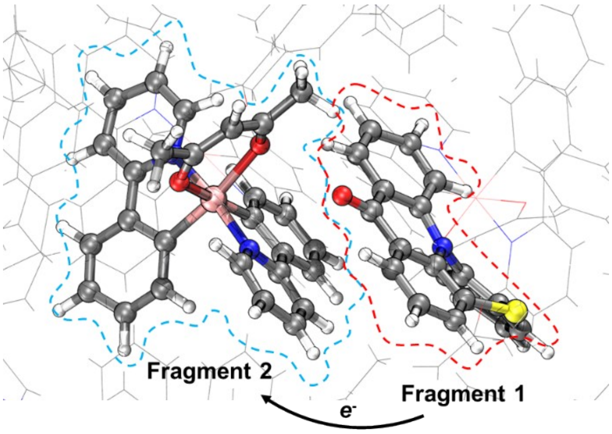

Net charge	Fragment 1	Fragment 2
T_1	-0.86	+0.86
S_0	0.00	0.00

Figure S22. Net charge on the two molecules in the complex in T_1 and S_0 states.

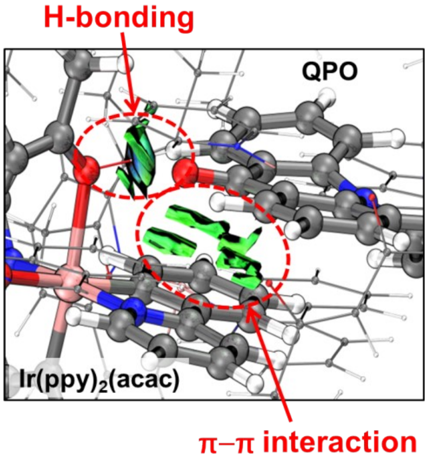

Figure S23. Intermolecular interactions within the host-guest system visualized by IGMH method.

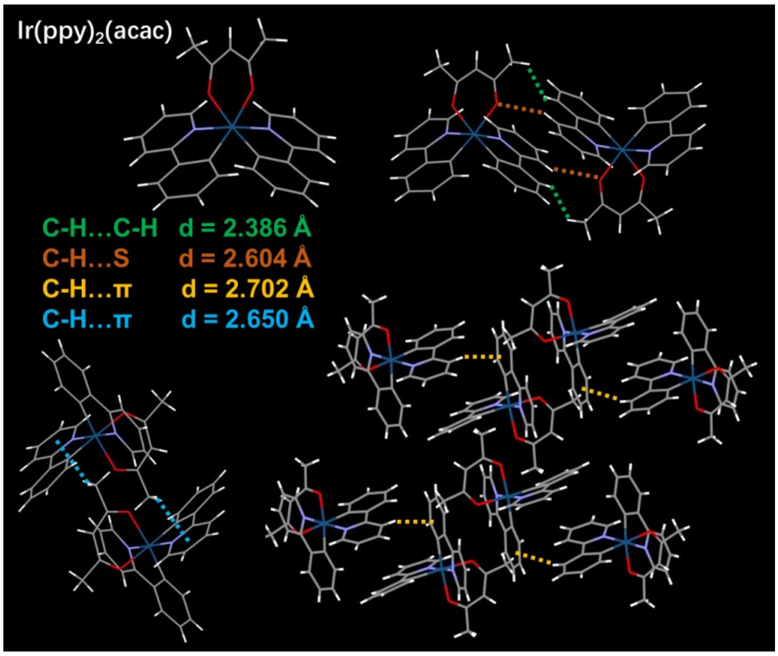

Figure S24. The molecular structure, intermolecular interactions, and packing modes of Ir(ppy)$_2$(acac) from single-crystal XRD.

References

[1] X. Wu, B.-K. Su, D.-G. Chen, D. Liu, C.-C. Wu, Z.-X. Huang, T.-C. Lin, C.-H. Wu, M. Zhu, E. Y. Li, W.-Y. Hung, W. Zhu, P.-T. Chou, *Nature Photonics* **2021**, *15*, 780-786.

[2] a) H. Bi, C. Huo, X. Song, Z. Li, H. Tang, S. Griesse-Nascimento, K.-C. Huang, J.-X. Cheng, L. Nienhaus, M. G. Bawendi, H.-Y. G. Lin, Y. Wang, S. K. Saikin, *The Journal of Physical Chemistry Letters* **2020**, *11*, 9364-9370; b) H. Zhang, L. Ke, Y. Nie, Z. Tu, J. Wang, S. K. Saikin, H. Bi, Y. Wang, *Physical Chemistry Chemical Physics* **2023**, *25*, 11102-11110; c) Y. Nie, H. Zhang, J. Wang, L. Ke, S. K. Saikin, H. Bi, W. Chen, G. Zhou, *Journal of Materials Chemistry C* **2024**, *12*, 7637-7643.

[3] W. Kohn, L. J. Sham, *Physical Review* **1965**, *140*, A1133-A1138.

[4] C. Adamo, V. Barone, *The Journal of Chemical Physics* **1999**, *110*, 6158-6170.

[5] a) S. Grimme, S. Ehrlich, L. Goerigk, *J Comput Chem* **2011**, *32*, 1456-1465; b) S. Grimme, J. Antony, S. Ehrlich, H. Krieg, *J Chem Phys* **2010**, *132*, 154104.

[6] a) F. Weigend, R. Ahlrichs, *Physical Chemistry Chemical Physics* **2005**, *7*, 3297-3305; b) F. Weigend, *Physical Chemistry Chemical Physics* **2006**, *8*, 1057-1065.

[7] G. W. T. M. J. Frisch, H. B. Schlegel, G. E. Scuseria, M. A. Robb, J. R. Cheeseman, G. Scalmani, V. Barone, G. A. Petersson, H. Nakatsuji, X. Li, M. Caricato, A. Marenich, J. Bloino, B. G. Janesko, R. Gomperts, B. Mennucci, H. P. Hratchian, J. V. Ortiz, A. F. Izmaylov, J. L. Sonnenberg, D. Williams-Young, F. Ding, F. Lipparini, F. Egidi, J. Goings, B. Peng, A. Petrone, T. Henderson, D. Ranasinghe, V. G. Zakrzewski, J. Gao, N. Rega, G. Zheng, W. Liang, M. Hada, M. Ehara, K. Toyota, R. Fukuda, J. Hasegawa, M. Ishida, T. Nakajima, Y. Honda, O. Kitao, H. Nakai, T. Vreven, K. Throssell, J. A. Montgomery, Jr., J. E. Peralta, F. Ogliaro, M. Bearpark, J. J. Heyd, E. Brothers, K. N. Kudin, V. N. Staroverov, T. Keith, R. Kobayashi, J. Normand, K. Raghavachari, A. Rendell, J. C. Burant, S. S. Iyengar, J. Tomasi, M. Cossi, J. M. Millam, M. Klene, C. Adamo, R. Cammi, J. W. Ochterski, R. L. Martin, K. Morokuma, O. Farkas, J. B. Foresman, and D. J. Fox, Gaussian, Inc., Wallingford CT, 2016.

[8] E. Runge, E. K. U. Gross, *Physical Review Letters* **1984**, *52*, 997-1000.

[9] a) C. Bannwarth, E. Caldeweyher, S. Ehlert, A. Hansen, P. Pracht, J. Seibert, S. Spicher, S. Grimme, *Wiley Interdiscip. Rev.-Comput. Mol. Sci.* **2021**, 11, 49; b) C. Bannwarth, S. Ehlert, S. Grimme, *Journal of Chemical Theory and Computation* **2019**, 15, 1652-1671; c) S. Grimme, C. Bannwarth, P. Shushkov, *Journal of Chemical Theory and Computation* **2017**, 13, 1989-2009; d) P. Pracht, F. Bohle, S. Grimme, *Physical Chemistry Chemical Physics* **2020**, 22, 7169-7192.

[10] a) Z. Shuai, *Chinese Journal of Chemistry* **2020**, *38*, 1223-1232; b) Z. Shuai, Q. Peng, *Physics Reports-Review Section of Physics Letters* **2014**, *537*, 123-156; c) Z. Shuai, Q. Peng, *National Science Review* **2017**, *4*, 224-239; d) Y. Niu, W. Li, Q. Peng, H. Geng, Y. Yi, L. Wang, G. Nan, D. Wang, Z. Shuai, *Molecular Physics* **2018**, *116*, 1078-1090.